Research article

Novel quinoline-4-carboxamide derivatives potentiates apoptosis by targeting PDK1 to overcome chemo-resistance in colorectal cancer: Theoretical and experimental results

Shalini V [a], Priyadarshini A N [c], Harsha Kachigere B [b], Vinay Kumar D C [d,f], Darshini Gowda [a], Chethan B S [d,e], Sudhanva M Srinivasa [c], Shobith Rangappa [c,**], Kanchugarakoppal S Rangappa [a,*]

[a] Department of Studies in Chemistry, Manasagangotri, University of Mysore, Mysuru, 570 006, Karnataka, India
[b] Department of Chemistry, Mysore University School of Engineering, Manasagangotri, University of Mysore, Mysuru, 570 006, Karnataka, India
[c] Adichunchanagiri Institute for Molecular Medicine, Adichunchanagiri Institute of Medical Sciences, Adichunchanagiri University, BG Nagara, 571 448, Karnataka, India
[d] Department of Studies in Physics, University of Mysore, Manasagangotri, Mysuru, 570 006, Karnataka, India
[e] Department of Basic Sciences, Amruta Institute of Engineering and Management Sciences, Bidadi, Bengaluru, 562 109, Karnataka, India
[f] Department of Physics, GSSS Institute of Engineering and Technology for Women, Mysuru, 570 016, Karnataka, India

ARTICLE INFO

ABSTRACT

A series of novel N,2-diphenyl-6-(aryl/heteroaryl)quinoline-4-carboxamide derivatives were designed and synthesized using the Suzuki coupling reaction and evaluated them for their anti-cancer activity. These compounds were screened for anti-colon cancer activity through *in-silico* studies by molecular docking and molecular dynamics studies. Furthermore, the density functional theory was used to determine the molecule's electrical properties. The molecular electrostatic potential map is used to evaluate the charge distribution on the molecule surface. Unveiling that the compound **7a** (binding energy of −10.2 kcal/mol) has good inhibition activity compared to other synthesized compounds (**7b-7j**) as well as the standard drug Gefitinib. The stability of the compound **7a** with the 1OKY protein was confirmed through molecular dynamics simulation studies, indicating potential anti-colon cancer activity against *phosphoinositide dependent protein kinase-1* (PDK1). The *in-silico* ADMET pharmacokinetic properties indicate adherence to Lipinski's rule of five for favorable safety profiles and the compound falls within the optimal range for physicochemical and pharmacokinetic properties, which is comparable to that of the standard medication drug Gefitinib. The synthesized library of compounds was further evaluated for their *in-vitro* anticancer potency against colon, pancreatic and breast cancer cells. The results demonstrated that the compounds effectively suppressed the proliferative potential of the screened cells in a concentration-dependent manner, as revealed by MTT assay. The anticancer potential of these molecules was further evaluated by acridine orange/PI, and Hoechst/PI which demonstrates the potential of molecules to induce apoptosis in cancer cells. Further investigations and optimization of these derivatives could lead to the development of effective anticancer strategies.

1. Introduction

Colon cancer, also known as colorectal cancer, is a significant health concern worldwide. According to Globocan survey, there were close to 20 million newly estimated cases in the year 2022, with colorectal cancer accounting for 9.6 % of cases worldwide and also accounts for 9.3 % mortality worldwide [1]. Colon cancer is one of the most common types of cancer globally and it is particularly prevalent in developed countries such as the United States, Canada, Australia, and Western European nations. However, its incidence is rising in many low and middle-income countries as well. The risk of developing colon cancer increases with age and also with other risk factors such as family history, polyps, inflammatory bowel disease, obesity, a sedentary lifestyle, smoking, excessive alcohol consumption and a diet high in red and processed meats [2,3]. Screening for colorectal cancer is crucial for early detection and prevention, which can improve treatment outcomes and survival rates. The survival rates of colon cancer vary depending on the stage during diagnosis. Early-stage cancer has a high survival rate, while late-stage cancers have lower survival rates. Chemotherapy plays a key role in treating colorectal cancer, particularly for the advanced stage of the disease. The most common drug treatments for colorectal cancer include Fluorouracil (5-FU), Capecitabine, Oxaliplatin, and Irinotecan. Combinational drug treatment has proven beneficial for treating colorectal cancer such as combining Fluorouracil, Leucovorin, and Oxaliplatin (FOLFOX), Fluorouracil, Leucovorin, and Irinotecan (FOLFIRI), Capecitabine and Oxaliplatin (CAPEOX), Capecitabine and Irinotecan (CAPIRI) [4]. 5-Fluorouracil is a commonly used chemotherapy drug for treating colorectal cancer, often in combination with other chemo drugs. Although it is effective, it can cause severe adverse effect and toxicity, which vary in severity from patients to patients. The toxicity of 5-FU may be influenced by factors such as dosage, infusion, duration, genetic variations in metabolic enzymes and concurrent usage of other drugs. Cardiotoxicity and neurotoxicity are common toxicities associated with 5-FU treatment, either alone or in combination treatment regimens [5]. Cancer cells can develop resistance to conventional therapies over time, rendering them less effective. Therefore, the development of new drugs is crucial to address the side effects associated with the conventional treatments, overcome resistance mechanism and enhance the treatment efficiency. PDK1 plays critical role in activating PI3K/AKT/mTOR pathway, which plays central role in regulating cellular metastasis, cell proliferation, angiogenesis and cell survival. Overexpression of AKT pathway has been reported in various colorectal cancer cells and is associated with the development of resistance to conventional chemotherapy drugs, leading to tumour relapse. Overexpression of AKT pathway helps cancer cells evade apoptosis by phosphorylating BAD to activate BCl2 related proteins and up-regulating anti-apoptotic proteins. Targeting AKT pathway proteins and its upstream target proteins can enhance the effectiveness of drug and improve overall treatment outcome [6–13].

Drug design in the cancer therapeutics is developing a trend towards the development of the drugs towards the achievement of the
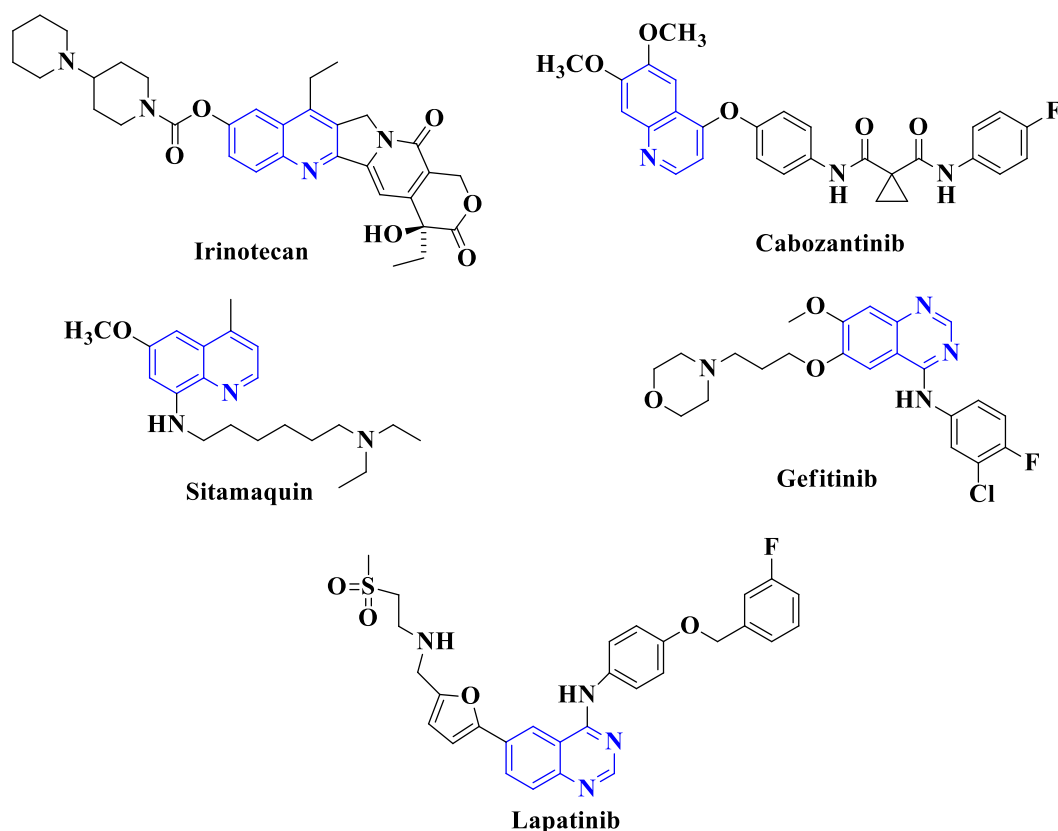

Fig. 1. The quinoline based drugs as anticancer agents.

more precise mechanisms of cancer cell destruction, thereby minimizing the adverse effects incurred during the course of the cancer treatment [14]. With the idea of the investigating the chemical substances having the properties to design novel anticancer agents, many class of the organic compounds have been identified. Special attention has been given to the quinolones and quinolines, which are the most common condensed heterocyclic aromatic compounds having the nitrogen in their structure and well known for their therapeutic potential [15,16]. Recently, numerous developments have been made in drug discovery, and as more the number of structures that are getting available, they are being tested for their pharmacological or biological properties using computational tools such as DFT, molecular docking and molecular dynamics studies.

Quinoline, also known as 1-aza-naphthalene, is a heterocyclic aromatic organic compound that has served as a potent pharmacophore in various approved drugs small molecules. FDA approved various quinoline-based drugs are antimalarial drugs (Chloroquine, Hydroxychloroquine, Mefloquine, Primaquine, Piperaquine), anti-cancer drugs (Lapatinib, Gefitinib, Irinotecan, Cabozantinib, Sitamaquin), antibacterial (Norfloxacin) (Fig. 1) [17]. Quinoline and its derivatives have garnered significant interest in medicinal chemistry and pharmacology due to their wide range of biological activities, including antimicrobial, antimalarial, anti-inflammatory, and anticancer effects. These effects are achieved by targeting specific signaling pathways, including apoptosis and inhibiting cell proliferation. Due to its versatility, quinoline derivatives hold promise for the development of new treatments for various diseases. Herein, we have endeavoured our sincere effort to synthesize a library of N,2-diphenyl-6-(aryl/heteroaryl)quinoline-4 carboxamide derivatives and evaluate their biological activity against a panel of cancer cells [18–24].

2. Materials and methods

2.1. Chemistry

Using Sorbent Technologies standard-grade silica gel, reaction products were purified using standard column chromatography (60–120 mesh). On Merck silica gel 60 F254 plates, analytical thin-layer chromatography was carried out. Visualization was accomplished with UV light. Melting points were recorded on a Thomas Hoover capillary melting point apparatus and are uncorrected. Proton nuclear magnetic resonance spectra (^{1}HNMR) were recorded on Agilent-400 MHz and Brucker-400 MHz and reported in ppm using CDCl$_3$ (7.24 ppm) and DMSO(3.33 ppm) as the internal standards. Proton-decoupled carbon nuclear magnetic resonance spectra (^{13}C NMR) were recorded on Brucker-100 MHz and Agilent-100 MHz, reported in ppm using CDCl$_3$ as the internal standard (77.0 ppm). Mass spectra were recorded on Waters' mass spectrum.

2.1.1. General procedure for the synthesis of quinoline-4-carboxylic acid (3)
A solution of 5-bromoisatin **1** (1 mmol) and potassium hydroxide (4 mmol) were taken in ethanol, and the reaction mixture was kept for 5 min. To the above reaction mixture, appropriate acetophenone **2** (1.1 mmol) was added and refluxed for about 12h. The completion of the reaction was monitored by TLC, and after the completion of the reaction, it was allowed to cool. The solvent ethanol was evaporated under reduced pressure. The residue was acidified with 2N aqueous hydrochloric acid until the pH of the solution attains acidic condition. The precipitated solid was filtered and dried under vacuum to obtain the pure corresponding quinoline-4-carboxylic acid derivatives **3**.

2.1.2. General procedure for the synthesis of 6-bromo-N,2-diphenylquinoline-4-carboxamide derivatives (5)
To the solution of quinoline-4-carboxylic acid **3** (1 mmol) and Et$_3$N (2 mmol) taken in anhydrous dichloromethane under an ice bath, HOBT was slowly added (1.2 mmol), followed by the addition of EDCl (1.2 mmol) and allowed to stir for about 1 h. After an hour, anilines **4** (2 mmol) was added dropwise, and the solution was left for 16 h. The reaction mixture was then washed three times with 10 % citric acid, saturated NaHCO$_3$, and followed by brine solution. The combined organic layer was dried over anhydrous sodium sulphate, and the solvent was evaporated under reduced pressure. The crude product was purified by column chromatography to obtain the pure 6-bromo-N,2-diphenylquinoline-4-carboxamide derivatives **5(a–c)** as white solids.

2.1.3. General procedure for the synthesis of N,2-diphenyl-6-(aryl/heteroaryl) quinoline-4 carboxamide derivatives (7a-j))
Scaffold **5** (1 mmol), boronic acids **6** (1 mmol), and K$_2$CO$_3$ (3 mmol) are taken in a sealed tube in the presence of EtOH, H$_2$O, and dioxane (1:1:5) as a solvent mixture. The reaction mixture was degassed for 5 min with inert nitrogen gas to create an inert atmosphere, followed by the addition of bis(triphenylphosphine) palladium (II) dichloride (0.1 mmol). Then the reaction mixture was kept for 30 min at 120 °C. The completion of the reaction was monitored by the TLC. After completion, the reaction mass was filtered under a Celite bed, followed by the removal of ethanol from the filtrate under reduced pressure. Then, the reaction mixture was extracted three times with EtOAc, followed by washing with water and brine solution. The combined organic layer was evaporated under reduced pressure to get the crude product. The crude product was purified by column chromatography to obtain the pure desired *N*,2-diphenyl-6-(aryl/heteroaryl) quinoline-4 carboxamide derivatives **(7a–7j)**. The HRMS, ^{1}H NMR and ^{13}C NMR are for the final structures are provided in the supplementary file.

2.1.3.1. 2-(4-methoxyphenyl)-N,6-diphenylquinoline-4-carboxamide (7a). White solid; 80 % yield (Rf = 0.60 in hexane/EtoAc 70:30 v/v); MP: 228.1–230.6 °C; ^{1}H NMR (CDCl3, 400 MHz): 8.85 (s, 1H), 8.12–8.09 (m, 2H), 7.94–7.85 (m, 5H), 7.59–7.57 (m, 3H), 7.52–7.48 (m, 2H), 7.45–7.35 (m, 3H), 7.30–7.27 (m, 1H), 6.85–6.83 (m, 2H), 3.75 (s, 3H). ^{13}C NMR (CDCl3, 100 MHz):165.7, 161.1, 155.8, 147.6, 142.6, 139.7, 139.4, 138.0, 130.3, 129.8, 129.4, 129.3, 128.8, 128.6, 127.7, 127.3, 125.0, 122.9, 122.6, 120.2, 116.0, 114.1,

55.2; HRMS (ESI) [M+H]$^+$ calculated C$_{29}$H$_{23}$N$_2$O$_2$ 431.1759 found 431.1758.

2.1.3.2. 6-(5-Fluoro-2-methoxyphenyl)-2-(4-methoxyphenyl)-N-phenylquinoline-4-carboxamide (7b). White solid; 81 % yield (Rf = 0.61 in hexane/EtoAc 70:30 v/v); MP: 254.3–256.6 °C. ^{1}H NMR (CDCl$_3$, 400 MHz): 8.51 (s, 1H), 8.15–8.10 (m, 2H), 7.95–7.89 (m, 3H), 7.81 (d, *J* = 7.2Hz, 2H), 7.72 (s, 1H), 7.45–7.41 (m, 2H), 7.26–7.21 (m, 1H), 7.07–6.99 (m, 2H), 6.9 (d, *J* = 7.6 Hz, 3H), 3.80 (s, 3H), 3.75 (s, 3H). ^{13}C NMR (CDCl$_3$, 100 MHz):165.6, 161.1, 158.3, 156.1, 152.7, 147.7, 142.7, 137.8, 136.3, 132.2, 130.6, 129.2, 128.7, 125.1, 125.0, 122.6, 120.1, 117.7, 117.4, 116.1, 115.0, 114.8, 114.2, 112.3, 112.2, 56.1, 55.3; HRMS (ESI) [M+H]$^+$ calculated C$_{29}$H$_{24}$FN$_2$O$_3$ 479.1771 found 479.1770.

2.1.3.3. 6-(5-Chloro-2-fluorophenyl)-2-(4-methoxyphenyl)-N-phenylquinoline-4-carboxamide (7c). White solid; 82 % yield (Rf = 0.58 in hexane/EtoAc 70:30 v/v); MP: 258.9–259.4 °C. ^{1}H NMR (CDCl$_3$, 400 MHz): 8.94 (s, 1H), 8.05–8.04 (m, 2H), 7.93 (d, *J* = 7.6 Hz, 2H), 7.86 (d, *J* = 8.8Hz, 1H), 7.80 (d, *J* = 8.4Hz, 2H), 7.54–7.47 (m, 5H), 7.42–7.35 (m, 3H), 7.29–7.25 (m, 1H), 3.72 (s, 3H). ^{13}C NMR (CDCl$_3$, 100 MHz):165.7, 161.1, 155.7, 147.5, 142.6, 139.6, 139.3, 138.1, 130.1, 129.7, 129.3, 128.8, 128.5, 127.7, 127.3, 125.0, 122.8, 122.5, 120.2, 115.9, 114.1, 55.2; HRMS (ESI) [M+H]$^+$ calculated C$_{29}$H$_{21}$ClFN$_2$O$_2$ 483.1276 found 483.1274.

2.1.3.4. 6-(4-chlorophenyl)-2-(4-methoxyphenyl)-N-phenylquinoline-4-carboxamide (7d). White solid; 82 % yield (Rf = 0.62 in hexane/EtoAc 70:30 v/v); MP: 261.2–263.5 °C. ^{1}H NMR (CDCl$_3$, 400 MHz): 8.33 (s, 1H), 8.26 (d, *J* = 2Hz, 1H), 8.20–8.18 (m, 1H), 8.06–8.04 (m, 2H), 7.93 (dd, *J$_1$* = 2Hz, *J$_2$* = 2Hz, 1H), 7.85–7.83 (m, 3H), 7.59–7.57 (m, 2H), 7.52–7.48 (m, 2H), 7.44–7.42 (m, 2H), 7.30–7.27 (m, 1H), 6.99–6.97 (m, 2H), 3.86 (s, 3H). ^{13}C NMR (CDCl$_3$, 100 MHz): 165.6, 161.2, 156.0, 147.8, 142.6, 138.14, 138.11, 137.8, 134.0, 130.3, 129.7, 129.44, 129.40, 129.0, 128.6, 128.5, 125.2, 122.9, 122.5, 120.2, 116.1, 114.2, 55.3; HRMS (ESI) [M+H]$^+$ calculated C$_{29}$H$_{22}$ClN$_2$O$_2$ 465.1370 found 465.1380.

2.1.3.5. 2-(4-methoxyphenyl)-N-phenyl-6-(thiophen-2-yl)quinoline-4-carboxamide (7e). White solid; 74 % yield (Rf = 0.66 in hexane/EtoAc 70:30 v/v); MP: 223.5–227.2 °C. ^{1}H NMR (CDCl$_3$, 400 MHz): 8.63 (s, 1H), 8.08–8.06 (m, 1H), 7.95–7.84 (m, 6H), 7.69–7.63 (m, 2H), 7.55–7.46 (m, 3H), 7.40–7.36 (m, 1H), 7.29–7.26 (m, 1H), 6.95–6.89 (m, 2H), 3.87 (s, 3H). ^{13}C NMR (CDCl$_3$, 100 MHz):165.7, 161.2, 156.1, 148.3, 142.6, 137.9, 130.6, 130.3, 129.34, 129.30, 129.2, 128.7, 128.6, 127.0, 125.0, 124.9, 122.6, 120.3, 120.2, 120.1, 115.7, 114.29, 114.24, 55.4; HRMS (ESI) [M+H]$^+$ calculated C$_{27}$H$_{21}$N$_2$O$_2$S 437.1324 found 437.1326.

2.1.3.6. 6-(2-Fluoro-5-methylphenyl)-2-(4-methoxyphenyl)-N-phenylquinoline-4-carboxamide (7f). White solid; 86 % yield (Rf = 0.68 in hexane/EtoAc 70:30 v/v); MP: 247.6–249.8 °C. ^{1}H NMR (CDCl$_3$, 400 MHz): 8.59 (s, 1H), 8.26 (s, 1H), 8.20–8.17 (m, 2H), 8.03–8.01 (m, 2H), 7.87–7.79 (m, 5H), 7.52–7.48 (m, 3H), 7.31–7.29 (m, 1H), 6.97–6.95 (m, 2H), 3.86 (s, 3H), 2.35 (s, 3H). ^{13}C NMR (CDCl$_3$, 100 MHz):165.5, 161.3, 156.4, 148.0, 143.1, 143.0, 142.5, 140.4, 140.4, 137.7, 135.2, 130.5, 130.3, 129.4, 129.3, 128.7, 125.3, 123.0, 122.8, 120.2, 119.6, 116.4, 114.3, 55.3, 22.7; HRMS (ESI) [M+H]$^+$ calculated C$_{30}$H$_{24}$FN$_2$O$_2$ 463.1822 found 463.1823.

2.1.3.7. 6-(6-Chloro-5-methylpyridin-3-yl)-2-(4-methoxyphenyl)-N-phenylquinoline-4-carboxamide (7g). White solid; 78 % yield (Rf = 0.66 in hexane/EtoAc 70:30 v/v); MP: 274.7–275.6 °C. ^{1}H NMR (CDCl$_3$, 400 MHz): 8.57 (s, 1H), 8.46–8.45 (m, 1H), 8.22–8.16 (m, 2H), 8.04–8.02 (m, 2H), 7.88–7.82 (m, 4H), 7.74 (m, 1H), 7.52–7.48 (m, 2H), 7.31–7.29 (m, 1H), 6.98–6.96 (m, 2H), 3.87 (s, 3H), 2.44 (s, 3H). ^{13}C NMR (CDCl$_3$, 100 MHz): 165.5, 161.4, 156.5, 151.0, 148.1, 145.3, 142.5, 137.8, 137.6, 134.9, 134.6, 132.5, 130.4, 129.4, 129.1, 128.7, 125.3, 123.0, 120.2, 116.4, 114.3, 55.4, 19.6. HRMS (ESI) [M+H]$^+$ calculated C$_{29}$H$_{23}$ClN$_3$O$_2$ 480.1479 found 480.1480.

2.1.3.8. N,2,6-triphenylquinoline-4-carboxamide (7h). White solid; 88 % yield (Rf = 0.68 in hexane/EtoAc 70:30 v/v); MP: 238.3–241.9 °C. ^{1}H NMR (CDCl$_3$, 400 MHz): 8.36 (d, *J* = 1.2Hz, 1H), 8.25–8.23 (m, 2H), 8.12–8.11 (m, 2H), 8.015 (dd, *J$_1$* = 1.6Hz, *J$_2$* = 1.6Hz, 1H),7.93 (s, 1H), 7.83–7.81 (m, 2H), 7.69–7.67 (m, 2H), 7.53–7.40 (m, 8H), 7.28–7.25 (m, 1H); ^{13}C NMR (CDCl$_3$, 100 MHz):165.6, 156.4, 147.9, 142.7, 140.0, 139.8, 138.2, 137.7, 130.1, 130.0, 129.9, 129.3, 128.96, 128.94, 127.9, 127.5, 127.3, 125.2, 123.3, 122.5, 120.2, 116.6; HRMS (ESI) [M+H]$^+$ calculated C$_{28}$H$_{21}$N$_2$O 401.1654 found 401.1657.

2.1.3.9. 6-(5-Fluoro-2-methoxyphenyl)-N,2-diphenylquinoline-4-carboxamide (7i). White solid; 84 % yield (Rf = 0.66 in hexane/EtoAc 70:30 v/v); MP: 264.2–265.7 °C. ^{1}H NMR (CDCl$_3$, 400 MHz): 8.37 (s, 1H), 8.31–8.30 (m, 1H), 8.22–8.20 (m, 1H), 8.11–8.09 (m, 2H), 7.97–7.95 (m, 2H), 7.79–7.77 (m, 2H), 7.55–7.42 (m, 6H), 7.29–7.24 (m, 1H), 7.15–7.12 (m, 1H), 7.08–7.03 (m, 1H), 3.79 (s, 3H). ^{13}C NMR (CDCl$_3$, 100 MHz):165.6, 158.3, 156.7, 152.7, 147.9, 138.5, 137.6, 132.2, 132.0, 131.9, 129.8, 129.3, 129.2, 128.9, 128.5, 128.4, 127.4, 125.14, 125.10, 123.0, 120.2, 117.7, 117.5, 116.7, 115.1, 114.9, 112.4, 112.3, 56.1. HRMS (ESI) [M+H]$^+$ calculated C$_{29}$H$_{22}$FN$_2$O$_2$ 449.1665 found 449.1652.

2.1.3.10. 6-(5-Fluoro-2-methoxyphenyl)-2-(4-fluorophenyl)-N-phenylquinoline-4-carboxamide (7j). White solid; 83 % yield (Rf = 0.64 in hexane/EtoAc 70:30 v/v); MP: 260.3–263.5 °C. ^{1}H NMR (CDCl$_3$, 400 MHz): 8.80 (s, 1H), 8.20 (m, 1H), 8.09–8.07 (m, 1H), 8.03–7.99 (m, 2H), 7.92–7.89 (m, 1H), 7.78–7.76 (m, 3H), 7.42–7.39 (m, 2H), 7.24–7.20 (m, 1H), 7.13–7.01 (m, 4H), 6.93–6.89 (m, 1H), 3.76 (s, 3H). ^{13}C NMR (CDCl$_3$, 100 MHz): 165.6, 165.2, 162.7, 158.3, 155.9, 155.3, 152.74, 152.73, 147.7, 142.7, 137.8, 136.78, 136.77, 134.53, 134.50, 132.2, 130.6, 130.5, 129.28, 129.21, 129.08, 125.1, 125.0, 122.8, 120.2, 117.7, 117.4, 56.1; HRMS (ESI) [M+H]$^+$ calculated C$_{29}$H$_{21}$F$_2$N$_2$O$_2$ 467.1571 found 467.1574.

2.2. In-silico studies

2.2.1. Density functional theory

The electron density distribution is the basis for all the compounds' physical and chemical characteristics, hence a wide range of theoretical investigations are employed to examine it. The synthesized compound's structure is utilized as the starting point for the first approximation that computes the electron wave functions. Density functional theory (DFT) was used to evaluate these wave functions using the B3LYP correlation functional and the 6-311G(d,p) basis set. The geometrical coordinates of the structure were optimized using the same theoretical level, and the self-consistent ground state configuration of the structure was shown by the absence of the imaginary frequencies.

The Koopman's approximation was used to estimate the energy gap of the compound's frontier molecular orbitals (HOMO and LUMO) to get more insight into its electronic characteristics. Additional parameters like the ionization energy, global softness, global hardness, chemical potential, electronegativity, etc. were also calculated based on the energy gap. The charge distribution is shown by the molecular electrostatic potential (MEP) map analysis, which also uses colour-coding from red to dark blue ((nucleophilic areas) blue > green > yellow > orange > red (electrophilic regions)) to anticipate probable reactive sites displayed by the chemical [25].

2.2.2. ADMET analysis

SwissADME and the pkCSM web server were used in the in-silico ADMET analysis to investigate the pharmacokinetic characteristics of the drug. The properties of ADMET (absorption, distribution, metabolism, excretion, and toxicity) were computed. The compound is assessed theoretically for numerous properties related to drug development and discovery, including hydrophilicity, hydrophobicity, solvent-accessible surface area, number of rotatable bonds, donor-hydrogen bonds, acceptor-hydrogen bonds, cytochrome P4502D6 binding (CYP2D6), hepatotoxicity, and skin permeability. Furthermore, the permeability of the BBB, Caco-2 cell, human intestinal absorption (HIA), skin permeability, cytochrome P4502D6 binding (CYP2D6), hepatotoxicity, and plasma protein binding (PPB) are all considered [26–28].

2.2.3. Molecular docking

Molecular docking is a computational technique for drug development that involves estimating the most likely binding site and evaluating the binding affinity in terms of binding energy related to organic compounds against protein targets, predicting ligand conformation pose. Flexible protein-ligand docking was performed using the 3D crystal structure of PDK1 (PDB ID: 1OKY), with resolution of 2.30 Å) from RCBS PDB database. The crystallographic structures of the PDK1 protein and ligand structures are prepared and optimized using molecular modelling software MGL tools 1.5.6 with Auto DockVina and Auto Dock Tools [29–31] and were prepared for molecular docking by removing water and co-crystallized ligands and polar hydrogens and Kollman charges were added to the energy-minimized protein as well as to convert target proteins and compound to the PDBQT format.

For the protein 1OKY the centre of the grid box was set to 88.345125 × 24.137750 × −2.851000 in the x, y, and z directions with the grid spacing of 0.395 Å, having a default grid box size of 56 × 65 × 72. The most likely ligand binding mechanism was determined by analyzing the docking findings and the intensity of the contacts was estimated by computing the binding energy, which is a negative score with the unit of kcal/mol. A technique used to examine molecular behaviour on target protein binding, the protein-ligand interactions were visualized and analyzed using Biovia Discovery Studio 2019 Client visualizer and the PyMOL Molecular Graphics System, Version 2.0 Schrödinger, LLC utilized in the search for new drugs [32–34].

2.2.4. Molecular dynamics

Molecular docking was effectively utilized to investigate various binding poses of the compound with the selected protein. However, the protein was treated as a rigid molecule during docking studies, thus not accounting for conformational changes [35]. To explore the conformational change during protein-ligand interactions, molecular dynamic (MD) simulations were performed. The MD simulations for the protein-ligand complex that included the compound **7a** was docked against PDK1 (PDB ID: 1OKY). The system was solvated using TIP3P water molecules and atomic interactions were evaluated with OPLS3 force field. A minimal quantity of Na+ and Cl− ions (0.15 M) was added to maintain the electrical neutrality, followed by the selection of an orthorhombic crystal system (dimensions: 10.0 × 10.0 × 10.0 Å), energy minimization, and equilibration using NPT ensemble model with temperature and pressure set at 300 K and 1.01325 bar, respectively. Desmond modules of the Schrödinger 2020-4 suite program were utilized for MD simulation analysis. The input and output results were visualized through Maestro structural visualization software tool [36,37].

2.3. In-vitro studies

2.3.1. Cell lines and culture condition

Human colon cancer cells, HCT116; Human cervical cancer cells, HeLa; Human triple negative Breast cancer cells, MDA-MB-231; Human Pancreatic adenocarcinoma cells, MIAPaCa2; were procured from National centre for Cell Sciences (NCCS), Pune, India. Human normal kidney cell lines, HEK; was a generous gift from Prof. Sathees C. Raghavan, the cell lines were authenticated by STR analysis recommended by ATCC and the cells were tested for mycoplasma contaminations by RTPCR analysis for 16S rRNA coding region and DAPI staining. Cells were cultured in IMDM, DMEM, L15 and DMEM high glucose with 2 mM L-glutamine and 1 mM Sodium pyruvate (Thermo Fisher Scientific, Inc.; Waltham, MA USA) containing 10 % FBS (Gibco; Grand Island, NY, USA). Cells were cultured in a humidified Incubator with and without 5 % CO_2 at 37 °C.

2.3.2. MTT and trypan assay

The assay was performed as described previously [38], briefly cells were seeded into a 96-well plate and allowed to attach overnight. The cells were then treated with increasing concentrations of the compound. The cells were incubated for 48 h and subjected to the MTT and trypan assay. Trypan incubated cells were subjected to automated cell counter for cell counting. The absorbance of the solubilized formazan was measured at 570 nm using a microplate reader. A minimum of three independent experiments were conducted, and error bars were calculated.

2.3.3. Nuclear membrane deformation by Hoechst/PI (propidium iodide) staining

Hoechst/PI double staining assay was performed as described briefly [38], HCT116 cells were seeded into 6 well plates, incubated overnight and treated with increasing concentration of compound and allowed to incubate for 48h. Cells were collected, washed with PBS and subjected to Apoptotic analysis by Hoechst/PI double staining and imaged.

2.3.4. Apoptotic analysis by acridine orange/PI dual staining

HCT116 cells were seeded into six well plate, incubated overnight and treated with increasing concentration of compound and allowed to incubate for 48h. Cells were collected, washed with PBS and subjected to apoptotic analysis by Acridine orange/PI double staining and imaged.

2.3.5. Foci formation assay

The Foci formation assay was performed as described [39] briefly, HCT116 cells were seeded and incubated overnight, then treated with increased concentrations of compound. The cells were incubated for 12 days with intermittent media change to replenish nutrients, followed by crystal violet staining for analyzing the colonies.

3. Results and discussion

3.1. Synthesis of N,2-diphenyl-6-(aryl/heteroaryl)quinoline-4-carboxamide derivatives

5-Bromoisatin **1** undergoes condensation reaction with different substituted acetophenone derivatives in the presence of KOH and ethanol as a solvent under reflux conditions to afford the desired quinoline-4-carboxylic acid derivatives in 90 % yield. In the next step, quinoline-4-carboxylic acid derivatives **3** were reacted with aniline **4** in the presence of triethyl amine, EDCl, HOBT, and DCM as solvents to get the respective scaffolds 6-bromo-N,2-diphenylquinoline-4-carboxamide derivatives **5** in an 80 % yield. The scaffolds **5** react with various electronically diversified boronic acids **6** via Suzuki coupling in the presence of K_2CO_3, Dikis and EtOH, H_2O and 1,4-dioxane as solvent mixtures in the ratio of 1:1:5 to afford the novel derivatives of N,2-diphenyl-6-(aryl/heteroaryl) quinoline-4-carboxamide derivatives **7a-7j** (Scheme 1) in good to moderate yields and the results are summarized in (Fig. 2).

3.2. In-silico studies

3.2.1. Density functional theory

The frontier molecular orbital distribution of the compound **7a** is shown in Fig. 3a. It is observed that the HOMO is localized over
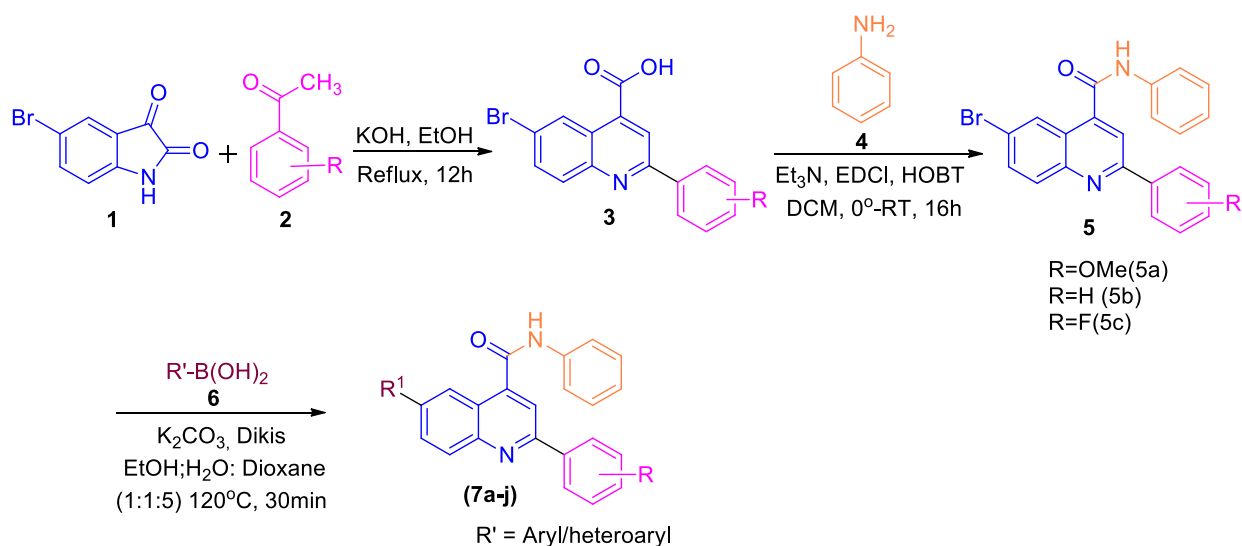
Scheme 1. Synthesis of N,2-diphenyl-6-(aryl/heteroaryl) quinoline-4-carboxamide derivatives **(7a-j)**.
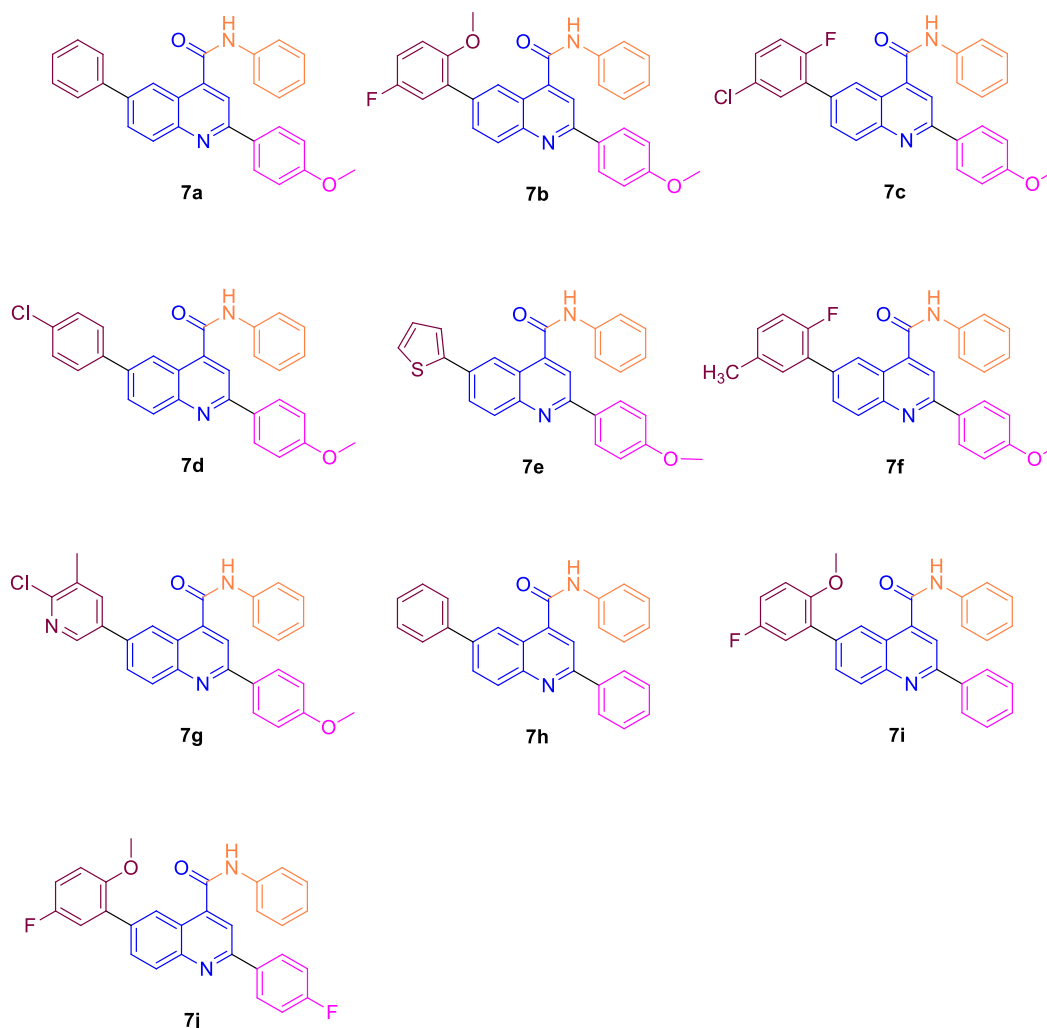
Fig. 2. Structure of newly synthesized *N,*2-diphenyl-6-(aryl/heteroaryl) quinoline-4-carboxamide derivatives.

the region of the methoxy phenyl and diphenylquinoline ring, whereas the LUMO is the methoxyphenyl diphenylquinoline and carboxamide moiety. The LUMO energy is proportional to its electron affinity, whereas the HOMO energy is related to its ionization potential. The positive phase is represented by the color red, whereas the color green represents the negative phase. The molecule is soft, stable, and more reactive to chemicals, as evidenced by the 3.259 eV energy difference between the HOMO and LUMO orbitals [40]. A molecule's electrophilic potential for biological action is indicated by its electrophilicity (ω) [41]. The dipole moment's high value is encouraging for more interactions with the proteins. The computed energies of many molecular reactivity characteristics for the **7a** molecule are displayed in Table 1. We can determine the chemical characteristics of the substance thanks to the global quantum chemical frontier molecular orbital energy descriptors [42].

The charge distribution on the molecule may be seen in terms of color grading by using the electrostatic surface potential map. Additionally, it discloses the electropositive and electronegative regions connected to the molecule, as well as details the physiochemical characteristics of the molecules. These areas aid in the identification of possible binding locations. The MEP of the **7a** molecule clearly demonstrates the presence of a large negative potential region (red colored) around the oxygen atoms of the carboxamide moiety and methoxyphenyl group (O1, and O2), which is prone to the electrophilic attack shown in the structure (Fig. 3b). While the blue surface formed on the hydrogen atoms demonstrates they're electropositive. Nonetheless, their intermolecular interactions are shown by the light yellow zone that formed on the MEP surface as a result of a possible halfway point between the two extreme locations.

3.2.2. Molecular docking analysis for the protein 1OKY

All the compounds (**7a to 7j**) were screened for *in-silico* molecular docking analysis; in this, it was found that all the compounds were found to be good inhibitors of the PDK1 protein. The corresponding binding score and interacting amino acids with their distances are summarized in Table 2. The surface view of the lowest conformer with the best docking pose of all the molecules **(7a–7j)**
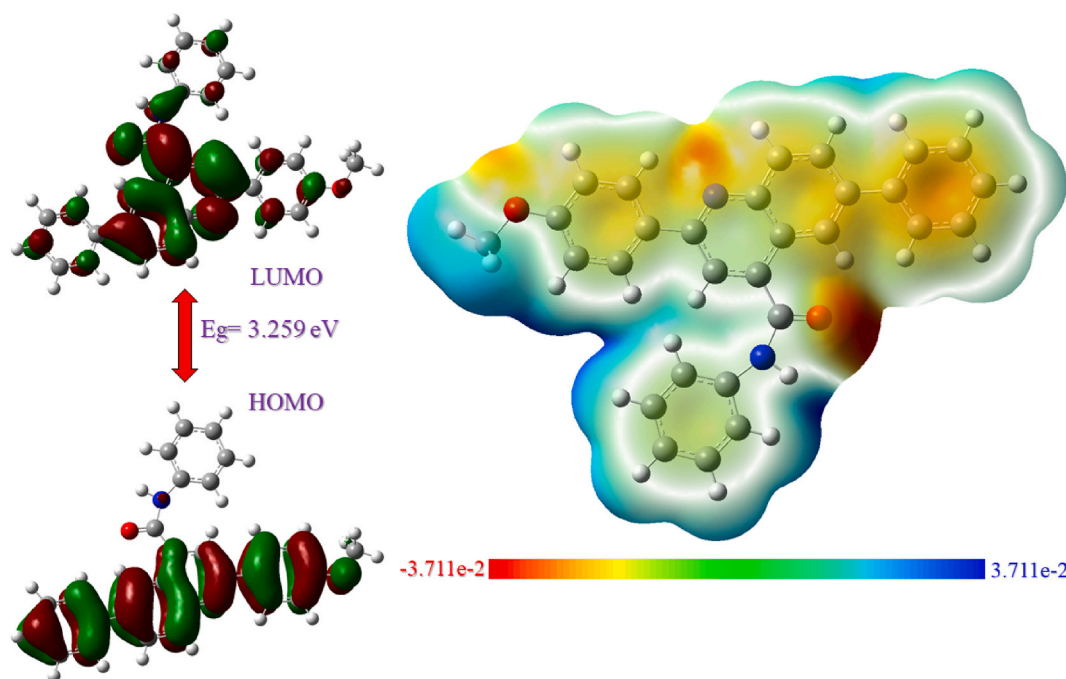
Fig. 3. (a) Frontier molecular orbital distribution, (b) Molecular electrostatic potential map of the 7a compound revealing the electrophilic and nucleophilic regions.

Table 1
The HOMO-LUMO energy and quantum chemical parameters of the 7a compound.

Parameter	Value
E_{HOMO} (E_H eV)	−5.8205
E_{LUMO} (E_L eV)	−2.5609
Energy gap ($Eg = E_H - E_L$ eV)	3.2597
Ionization energy ($I = -E_H$ eV)	5.8205
Electron Affinity (A) ($A = -E_L$ eV)	2.5609
Electronegativity ($\chi = (I+A)/2$ eV)	4.1907
Chemical Potential ($\mu = -\chi$ eV)	−4.1907
Global hardness ($\eta = \Delta E/2$ eV)	1.6298
Global softness ($\sigma = 1/2\eta$ eV^{-1})	0.6136
Electrophilicity index ($\omega = \mu^2/2\eta$ eV)	5.3877
Dipole Moment in Debye	4.2336

with 1OKY protein and unveiling the 2D interactions with active site amino acids, represented by different colours for all the molecules are provided in Fig. S2 -.

The ligand (compound **7a**) was docked with the X-ray crystal structure of PDK1 (3-phosphoinositide dependent protein kinase-1) with PDB ID 1OKY protein to provide a detailed explanation and comprehensive evidence of the interaction between the small molecule and the active site residues of the target protein. Molecular docking results demonstrate the binding model between compound and protein with the most stable structure and binding energy of −10.2 kcal/mol. In the docked conformation of the inhibitor molecule (Fig. 4b), two hydrogen bonding interactions were observed between the oxygen atoms of amino acid residue TYR161 and the carbon atom at a distance of 3.71 Å. Additionally, the centroid of the phenyl ring attached to the quinoline moiety interacts with the amino acid THR222 at a distance of 3.68 Å, forming a π-donor hydrogen bond, with the oxygen atom in the amino acid acting as the donor. The o-methoxy group forms an π-alkyl bond between the carbon atom of the amino acid LEU88 at a distance of 3.79 Å. Further interactions was observed between the centroid of the phenyl ring and the N-containing phenyl ring in the quinoline moiety with the amino acids VAL96 at a distance of 3.80 Å, and LEU212 at distances of 3.98 Å, and 3.73 Å respectively. Interestingly, the centroid of the phenyl ring attached to the quinoline moiety forms a π-sulfur interaction with the sulfur atom of the amino acid MET134. Further, the molecule is also interacting with amino acid residues, namely, LYS111, ALA109, VAL96, LEU88, VAL96 of 1OKY protein, through π-π stacked interactions involving the centroid of the phenyl ring attached to the quinoline moiety, the centroid quinoline rings, the phenyl amide ring, and the phenyl methoxy ring, respectively. Molecular docking studies unveil the best-fit orientation of the molecule with the protein and are typically used to assess the interactions between them. Later, the molecular docking results of **7a-7j** were compared

Table 2
Showing the different interactions exhibited by all ten compounds **(7a -7j)** with the PDK1 protein with corresponding docking score and distances.

C#	Docking Score kcal/mol	Interacting amino acids	Type of interactions	Distance in Å
7a	−10.2	TYR161	Conventional H-bond	3.71
		THR222	π-donor H bond	3.68
		MET134	π-sulfur	5.88
		GLU90	Amide π-stacked	4.40
		VAL96, LEU88, LEU212	π-σ	3.80, 3.79, 3.73, 3.98
		ALA109, LYS111	π-alkyl	5.21, 4.84
SD	−7.1	ASP223	Conventional H-bond	5.35, 5.47
		ASP205	π-anion	7.78
		PHE242	π- π T shaped	6.20, 6.39
		LYS123	π-alkyl	5.54, 3.84
		PHE93	alkyl	4.55
7b	−10.0	LYS161, LYS86, GLU166, THR222	Conventional H-bond	3.57, 3.52, 3.33, 3.12
		GLY165, GLU130	C-H bond	3.46, 3.70
		THR222, LEU212	π-σ	3.76, 3.84
		LYS111, VAL96, LEU88, LEU212	π-alkyl	4.72, 4.29, 3.81, 5.46
7c	−9.8	VAL96, LEU212	π-σ	3.96, 3.81, 3.73
		GLU90, ALA109, LYS111	π-alkyl	4.55, 5.18, 4.95
		LEU88	π-alkyl	5.39, 4.69, 4.61
		VAL96	π-alkyl	5.03, 5.24
7d	−9.9	GLU166, THR222	Conventional H-bond	3.28, 3.06
		LEU88, LEU212, THR222	π-σ	3.77, 3.88, 3.77
		GLU130	C-H bond	3.71
		LEU88, LYS111	π-alkyl.	4.52, 4.66
		LEU212, VAL96	π-alkyl	5.47, 5.40, 4.28
7e	−10	THR222	π-donor H-bond	3.59
		MET134	π-sulfur	5.79
		GLU90	amide π- stacked	4.31
		VAL96, LEU212, LEU88	π-σ	3.85, 3.66, 3.98, 3.89
		LYS111, ALA109, LEU88	π-alkyl	4.86, 5.26, 4.88
		VAL96	π-alkyl	5.20, 5.44, 5.17
7f	−10.1	ASN210, GLY89	C-H bond	3.89, 3.57
		LEU212	π- donor H-bond	3.57
		LEU212, VAL96, ALA109, LEU212	π-alkyl	5.15, 4.44, 5.30, 5.14
		LEU88, LEU212		4.84, 4.16, 4.92, 5.34
7g	−9.8	GLU166, THR222	Conventional H-bond	5.78, 4.54
		GLU130	C-H bond	6.87
		LEU88, LEU212, THR222	π-σ	4.25, 5.57, 5.66
		LEU88, LEU212, VAL96,	π-alkyl	4.04, 6.82, 6.37, 4.96
		LYS111	π-alkyl	4.60
7h	−10.0	MET134	π-sulfur	8.98, 7.03
		GLU90	amide π- stacked	4.79, 3.84, 6.64, 5.78
		VAL96, LEU88, LEU212	π-σ	5.34, 6.51, 5.31, 4.98
		LYS111, ALA109, LEU88, VAL96	π-alkyl	6.03, 4.81
7i	−10.1	LYS86	Conventional H-bond	5.25
		LEU88, LEU212	π-σ	4.45, 5.69
		LYS86, LEU88	π-alkyl	5.18, 5.20, 3.95
		ALA109, LEU159, VAL143	π-alkyl	5.46, 650, 6.60
		VAL96	π-alkyl	5.21, 6.68, 5.75
7j	−9.4	SER92	Conventional H-bond	4.38
		GLU130	Halogen (fluorine)	5.30
		PHE242, PHE93	π- π stacked	4.94, 7.00, 4.58
		TYR126	π-cation	7.42, 5.24, 5.10
		LYS123, LYS123, VAL243	π-alkyl	5.24, 5.59, 5.06, 5.87

with the standard medication drug named Gefitinib (Fig. 6), which, interestingly, showed the binding energy of −7.1 kcal/mol as shown in Fig. 5 and Table 1. The results unveil the surface view, and the cartoon view of the molecule with 1OKY protein (Figs. 4–5). The ligand, which can inhibit the protein, acts as a small drug-like molecule that binds to the target protein.

3.2.3. Molecular dynamics simulation analysis

Molecular dynamic simulation studies were employed to acquire atomic level information about protein ligand interactions. Root-mean-square deviation (RMSD), root-mean-square fluctuation (RMSF), radius of gyration, and other protein-ligand complex contacts were computed to based on molecular dynamic trajectories to reveal details about the structural stability, binding modes, and binding strength of the designed drug molecule. The dynamic behavior of the protein-ligand system was observed over a 100 ns simulation period.
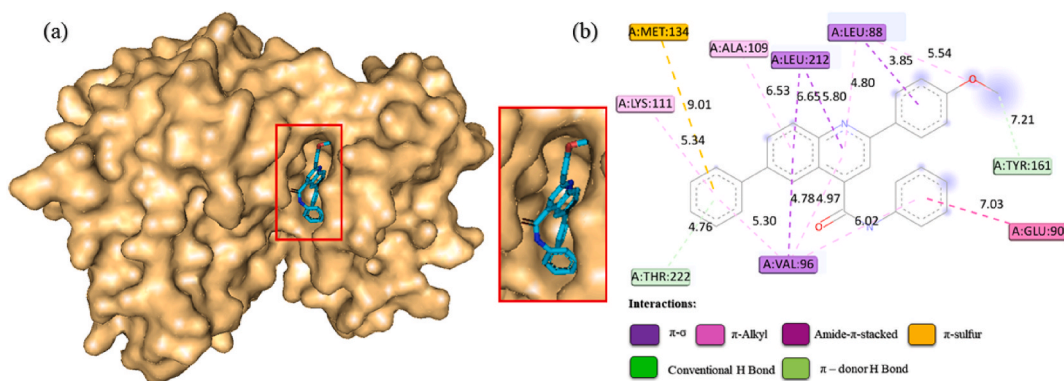
Fig. 4. Surface view of the lowest conformer with best docking pose of the molecule **7a** with 1OKY protein and unveiling the 2D interactions with active site amino acids are represented by different colours. (For interpretation of the references to color in this figure legend, the reader is referred to the Web version of this article.)
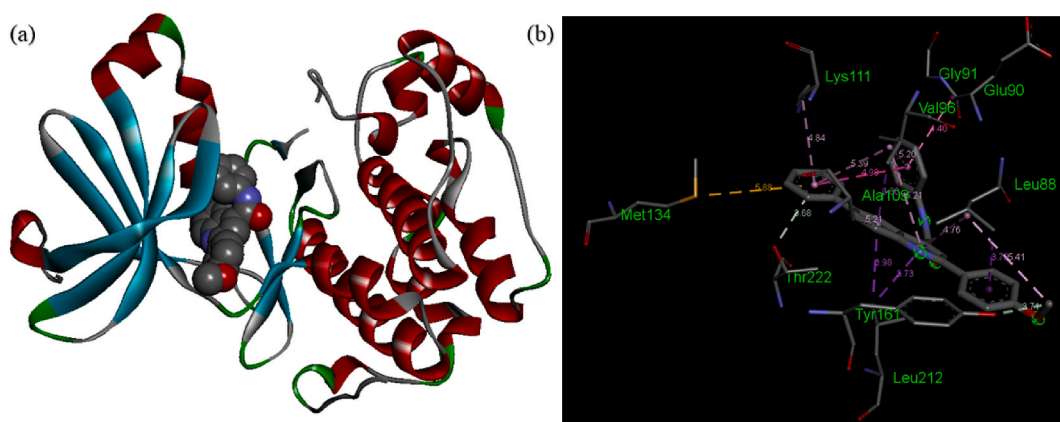

Fig. 5. Cartoon view of the lowest conformer with best docking pose of the molecule **7a** with 1OKY protein and corresponding amino acids interacting distances.

3.2.4. Enumerating conformational stability

The RMSD plots against simulation time for the suggested proteins with compound **7a** are shown in Fig. 7, which also demonstrates that the RMSD plots for Cα atoms of the backbones of the 1OKY-7a ligand complex. During the 100 ns simulation period, the protein-ligand complex experienced a large deviation until it reaches to 48 ns, after which the system settled into a relatively stable equilibrium with deviations of 5 Å at 60 ns. After 60 ns, the protein-ligand complex showed a slight disturbance in its equilibrium state until the end of the simulation period.

3.2.5. Residue flexibility analysis

The flexibility of the protein was evaluated by the RMSF parameter, which indicates the flexibility of the amino acid residues in the targeted proteins. In the 1OKY-ligand complex, the residues involved in the interactions with the ligand such as LYS86 (2.6 Å), ILE87 (2.41 Å), SER92 (4.33 Å), THR95 (2.01 Å), VAL97 (1.70 Å), GLU121 (3.45 Å), VAL124 (3.01 Å), THR128 (2.28 Å), ASP132 (1.87 Å), PHE242 (3.23 Å), VAL243 (3.27 Å) and THR245 (1.61 Å) shows highest fluctuations (Fig. 8).

3.2.6. Analysis of residue with ligand interactions

The analysis of the protein-ligand interactions offers in-depth insights into the pharmacodynamics, and pharmacokinetics of the investigational compounds. Several non-covalent interactions between the ligand and distinct amino acid residues within the protein enhance the stability of the protein-ligand complex throughout the molecular dynamics simulations. The proportion of each amino acid's involvement in stabilizing the complex can be quantified through a 2D histogram plot, which elucidates the interaction profile of the protein-ligand complex.

In the 1OKY-ligand complex, the ligand formed direct hydrogen bonds with the amino acid residues LYS86 (0.8 %), ILE87 (2.5 %), SER92 (5.0 %), LYS123 (5.0 %), TYR126 (1.6 %), ARG129 (0.5 %) and GLU166 (3.9 %). Major hydrophobic interactions were observed between the amino acids LYS86 (23.4 %), TYR126 (19.0 %), ARG129 (12.7 %), TYR161 (16.8 %), LEU212 (18.5 %) and VAL143 (7.4 %) and the ligand. Further, the amino acids LYS86 (6.3 %), GLU90 (5.8 %), ARG129 (8.2 %), TYR161 (8.7 %), TYR161
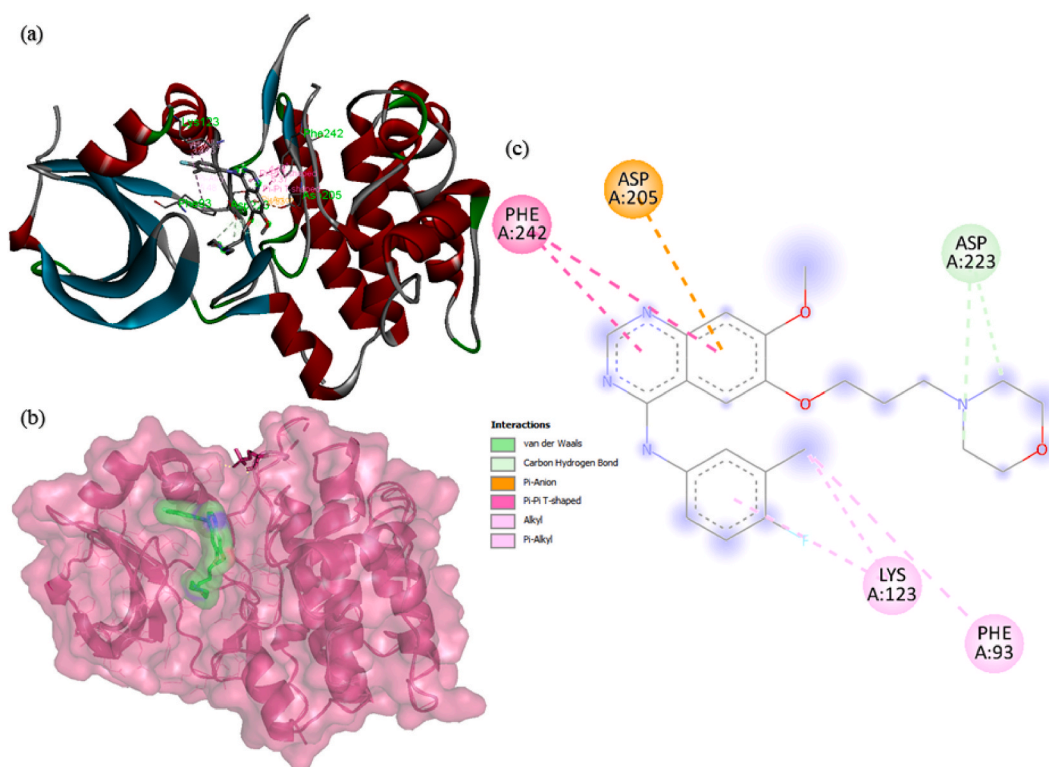
Fig. 6. Cartoon view and surface view of the docking of the standard drug Gefitinib with 1OKY protein and corresponding amino acids interactions.
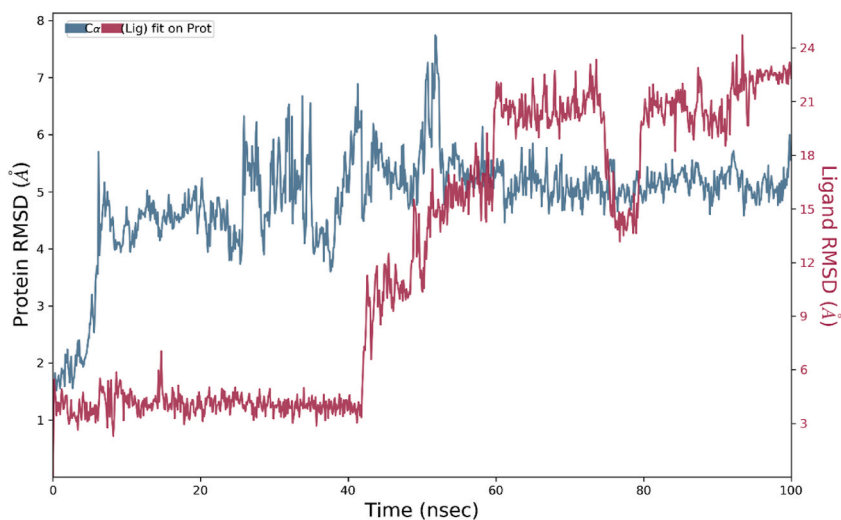

Fig. 7. RMSD plots of 1OKY-ligand complex over MD production run.

(8.7 %), GLU166 (13.2 %), GLU209 (21.9 %), GLY225 (8.4 %), and PHE224 (1.8 %) demonstrated significant water-bridged interactions. An ionic interaction was also observed between LYS123 and LYS86 with the ligand.

Green, violet, blue, and pink colours represent hydrogen bond, hydrophobic, water-bridged, and ionic interactions, respectively. The 2D histogram plot revealed that the water bridged interactions significantly contributed to the stabilization of the protein-ligand complex. Furthermore, it also provided information regarding the number of protein-ligand contacts formed at various stages during simulation process, considering the data obtained from the PL-contact timeline plot (a plot illustrating the number of protein-ligand contacts exhibited by various amino acids over time) (Fig. 9).

The conformational changes of each rotatable bond in the ligand throughout the simulation duration were characterized using the
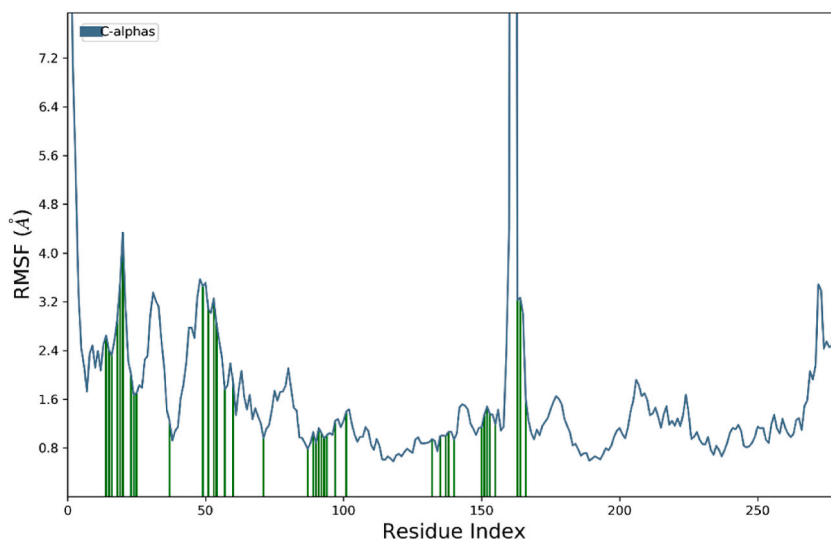
Fig. 8. RMSF plots of 1OKY-ligand complex over the period of 100 ns.

ligand torsion plot. The 2D representation of the rotatable bonds within the ligand is coded with different colours (Fig. 10). The torsion plot of each rotatable bond includes a radial plot and bar plots of the matching colours. Radial plots depict the torsion conformations throughout the simulation. The summarized data from the radial plots were depicted in bar plots (a plot of torsion potential as a function of the degree of freedom of rotation), which indicates the torsion probability density.

The synthesized compound exhibited six rotational bonds. The bonds between the ligand atoms were regarded as rotatable bonds and colour coded as dark green, violet, orange, pink, light green, and blue, respectively. The torsional freedom of each rotatable bond mentioned ranged from $-180°$ to $180°$. The 2D histogram and torsion plot of the ligand revealed that the ligand undergoes significant conformational adaptation to maintain a protein-bound conformation.

Furthermore, the stability of the ligand within the binding pocket of the selected protein was assessed by evaluating ligand properties throughout the simulation period (Fig. 11). For the 1OKY-ligand complex, the average values of RMSD, radius of gyration (rGyr), molecular surface area (MolSA), solvent accessible surface area (SASA), and polar surface area (PSA) were found to be 1.5 Å, 4.78 Å, 408 Å^2, 250.85 Å^2, and 82 Å^2, respectively. All the aforementioned properties contributed to the comprehension of the protein bound conformation of the complex, aligning with the previously obtained results.
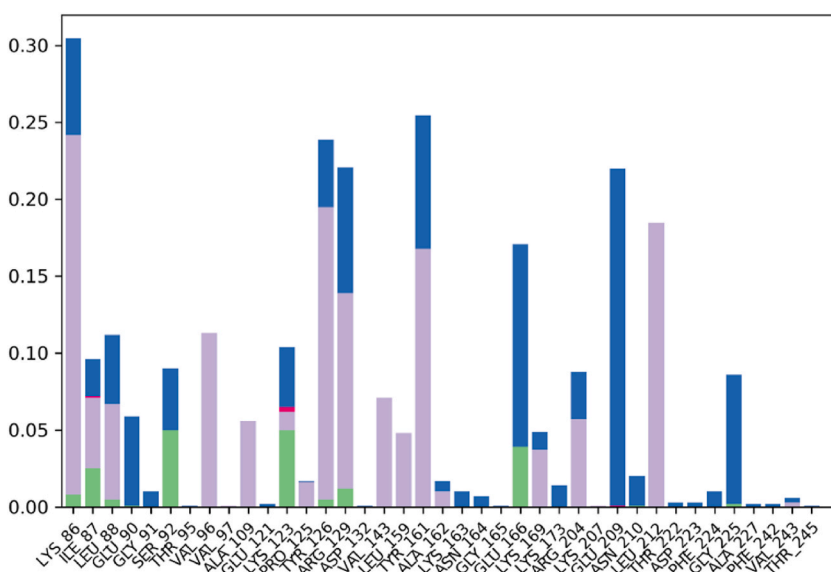

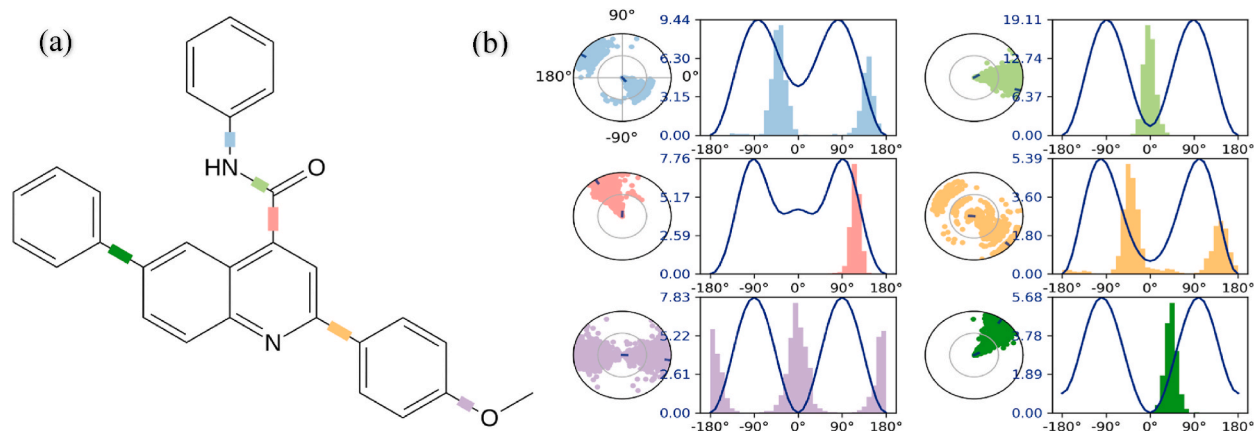**Fig. 9.** Protein-ligand contact maps of 1OKY-ligand complex and over the period of 100 ns.

Fig. 10. The 2D schematic of the rotatable bonds present in the ligand assigned with different colour codes for 1OKY-ligand complex over the period of 100 ns.
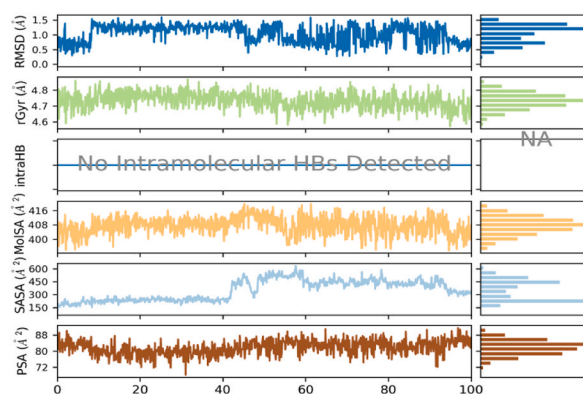

Fig. 11. RMSD, radius of gyration (rGyr), molecular surface area (MolSA), solvent accessible surface area (SASA), and polar surface area (PSA) of 1OKY-ligand complex.

3.3. In-vitro studies

3-Phosphoinositide dependent protein kinase-1 (PDK1) is a key regulatory protein in the PI3K/AKT pathway, which is primarily involved in activating downstream proteins such as AKT. The activated AKT pathway proteins regulate various cellular processes, including cell growth and proliferation, migration and invasion, angiogenesis, cell survival, and apoptosis. Overexpression of the AKT pathway has been reported in various colon cancer cells and results in acquired chemo-resistance against frontline chemotherapeutic agents. The development of targeted therapies for colon cancer has gained significant attention due to prevailing chemo-resistance.

3.3.1. Compound 7a regress cell proliferation and colony formation of colon carcinoma cells

Cancer cells display an inherent propensity to proliferate and multiply indefinitely, which results in the formation of a mass of undifferentiated cells. Anticancer small molecules regress the proliferation rate of cells and actuate apoptotic process in cancer cells. To evaluate the effect of the compound against the progression of colon cancer cells (HCT116), cells were treated with increased concentration of compound and subjected to MTT and trypan analysis. The results reveal the compound efficiently regresses the proliferation rate and viability of colon cancer cells in a concentration dependent manner, with IC$_{50}$ ranging from 35.67 μM to 48.31 μM (Table 3). Interestingly, compound exhibits less toxicity towards normal cell lines (HeK) (Fig. 12a and b). The ability of regressing colony formation was evaluated by subjecting to form colonies by foci formation assay, and the results demonstrated the potent inhibitory property of the compound to inhibit colony formation of colon cancer cells in a concentration dependent manner (Fig. 12c and d).

3.3.2. Compound 7a induces apoptosis of colon cancer cells

Cancer cells evade program cell death by altering various signaling pathways, targeting the tumor cells and inducing apoptosis is crucial to combating cancer cells. Various anticancer small molecules execute this process by targeting aberrantly over expressed proteins involved in signaling mechanism or by targeting crucial cellular proteins involved in maintaining homeostasis. To evaluate

Table 3

IC$_{50}$ values of synthesized library of compounds against panel of cancer and normal cells.

IC$_{50}$ (μM)

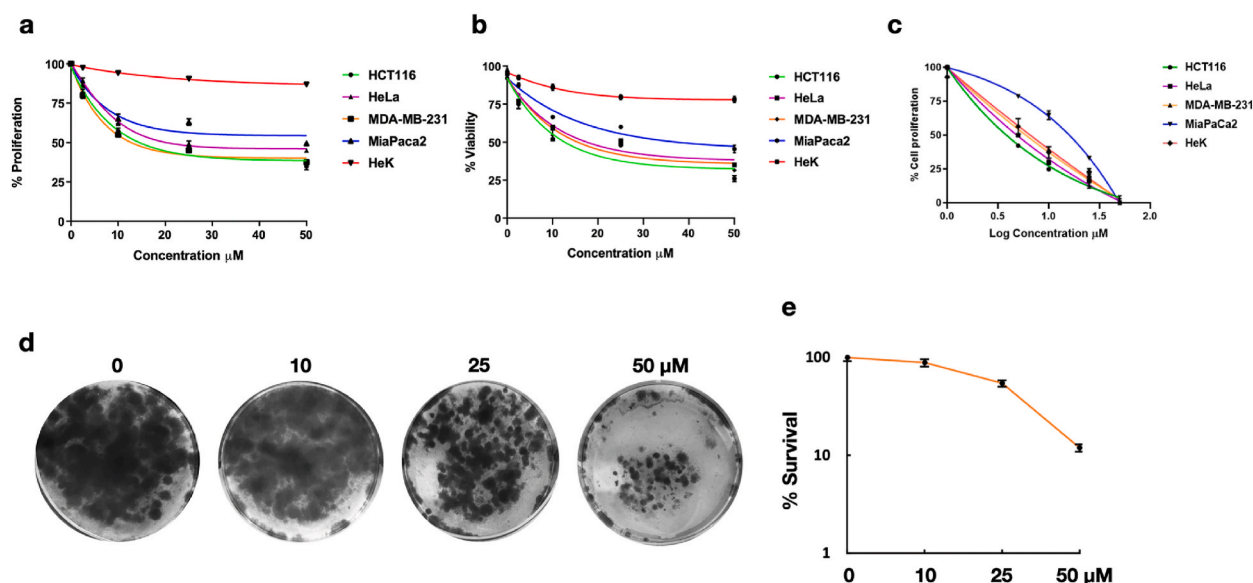| Compounds	HCT116	HeLa	MDA-MB-231	MIAPaCa2	HEK
7a	**35.6 ± 0.06**	**41.3 ± 0.06**	**39.2 ± 0.13**	**48.3 ± 0.13**	>50
7b	43.3 ± 0.53	41.6 ± 0.58	>50	>50	>50
7c	41.8 ± 0.16	42.4 ± 0.37	>50	>50	>50
7d	39.8 ± 0.11	38.3 ± 0.25	>50	>50	>50
7e	>50	>50	>50	>50	>50
7f	>50	>50	>50	>50	>50
7g	>50	>50	>50	>50	>50
7h	41.6 ± 0.11	43.3 ± 0.31	46.3 ± 0.18	>50	>50
7i	44.2 ± 0.08	>50	>50	>50	>50
7j	42.5 ± 0.23	>50	>50	>50	>50
Doxorubicin	1.26 ± 0.09	5.04 ± 0.41	5.32 ± 0.11	25.3 ± 0.21	8.23 ± 0.73

Fig. 12. Compound 7a effect on cell proliferation and colony formation: Cells treated with various concentration of compound subjected MTT and Trypan assay (a) Cell proliferation by MTT (b) percentage viability by trypan (c) Cell proliferation by MTT with Standard drug Doxorubicin (d) Foci formation assay(e) percentage survival graph. DMSO treated cells served as control. Each experiment was repeated thrice error bars were represent the SEM of control with treated groups.

the potency of compound to induce apoptosis the cells were exposed to increased concentration of compounds and subjected to Acridine orange/Propidium iodide dual staining to evaluate the live and dead cells after the compound treatment. The results clearly unveil that the compound treated cells displayed propidium iodide uptake in concentration dependent manner; live cells are stained with acridine orange with an intense green colour and dead cells are stained with propidium iodide with an intense red colour (Fig. 13a and b).

3.3.3. Compound 7a triggers nuclear deformation

The intact cell membrane and nuclear membrane integrity ensures the survivability or viability of cells. Cells undergoing programme cell death exhibits altered membrane integrity, which allows the penetration of propidium iodide into the cell. To evaluate the anticancer potential of compound, cells were exposed to various concentrations of compounds and subjected to Hoechst/Propidium iodide dual staining. The results clearly unveiled the uptake of propidium iodide in concentration dependent manner with nuclear membrane deformation in dead cells, reveals the induction of apoptosis in colon carcinoma cells by the compound (Fig. 14a and b).

3.3.4. Physicochemical and ADMET properties

Several physicochemical properties of the **7a** molecule is examined, including its partition coefficient (Log P), number of rotatable bonds (RB), molecular weight (MW), hydrogen bond donors (HBD), and hydrogen bond acceptors (HBA). These characteristics are compared with that of the clinically approved reference medication drug, Gefitinib, and are shown in Table S1 [2]. It has been found that all of these characteristics fall within a desirable range. The skin permeability (log Kp) value (−2.735 cm/s) indicates low skin
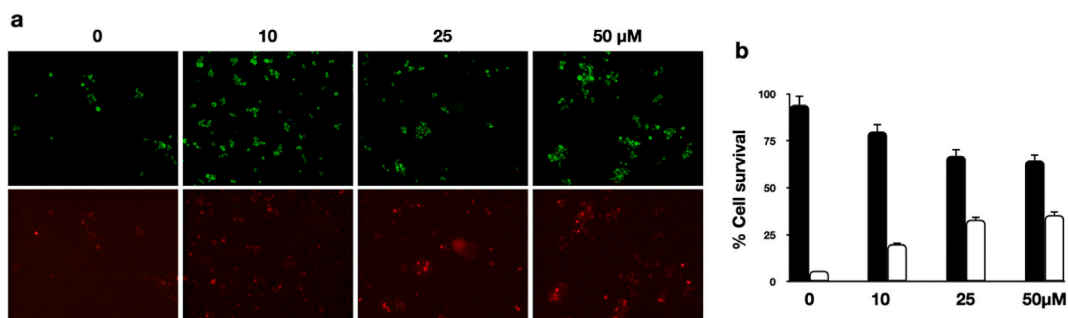
Fig. 13. Compound 7a effect on cell survival: cells treated with various concentration of compound subjected to acridine orange/Pi dual staining, (a) Acridine orange/PI dual staining images (b) histogram analysis of percentage survival cells. DMSO treated cells served as control. Each experiment was repeated thrice and minimum of 200 cells were counted and error bars were represent the SEM of control with treated groups. (For interpretation of the references to color in this figure legend, the reader is referred to the Web version of this article.)

absorption of the molecule. The molecule demonstrates a high intestinal absorption ability of 95.58 %, which is higher than that of the standard drug, which has an absorption ability of 92.63 %. For a given compound, a LogBB <1 indicates poor distribution to the brain, while LogBB >0.3 suggests the potential to cross BBB. LogPS >2 is considered indicative of compounds that can penetrate the CNS, while LogPS <3 suggest difficulty in crossing the CNS [3]. Thus, compound **7a** shows significant potential to cross the barrier. The compound **7a** is non-toxic to the dermis (skin sensitization) and found to be safe based on predictions of oral rat acute toxicity (**7a:** 3.436 mol/kg) and chronic toxicity (2-(4-methoxyphenyl)-N,6-diphenylquinoline-4-carboxamide): 1.393 log mg/kg_bw/day) and it is non-cytotoxic (hERG cell line). The compound inhibited all cytochrome P450 isomers (which regulate the drug metabolism), such as, CYP1A2, CYP2C19, and CYP2C9 except CYP7a4 and CYP2D6 (vital for the biotransformation of drug molecules). The compound **7a** has a synthetic accessibility score less than 4, which suggests that it can be easily synthesized. Drug-like predictions, including bioavailability scores and toxicity profiles, are provided in Table 4. 2-(4-methoxyphenyl)-N,6-diphenylquinoline-4-carboxamide compound falls within the optimal range for physicochemical and ADMET properties. As a result, the acquired ADMET score indicates that the drug molecule has generally favorable pharmacokinetics. Fig. 15 indicates both the boiled egg and bioavailability radar, which concludes that the molecule falls within the acceptable safety profile.

4. Conclusion

In summary, the present work highlights the promising potential of quinoline-4-carboxamide derivatives as a potent anticancer agent against panel of cancer cells, particularly in addressing chemo-resistance both by *in-vitro* and *in-silico* studies. The findings of the molecular docking and ADMET analysis indicated that the **7a** molecule had good drug likeness and excellent pharmacokinetic features, making it a suitable model for the development of anticancer drugs. The energy gap states the molecule is stable, chemically more reactive, and is equivalent to that of bioactive compounds. The potential applications of the **7a** molecule in biological and structural
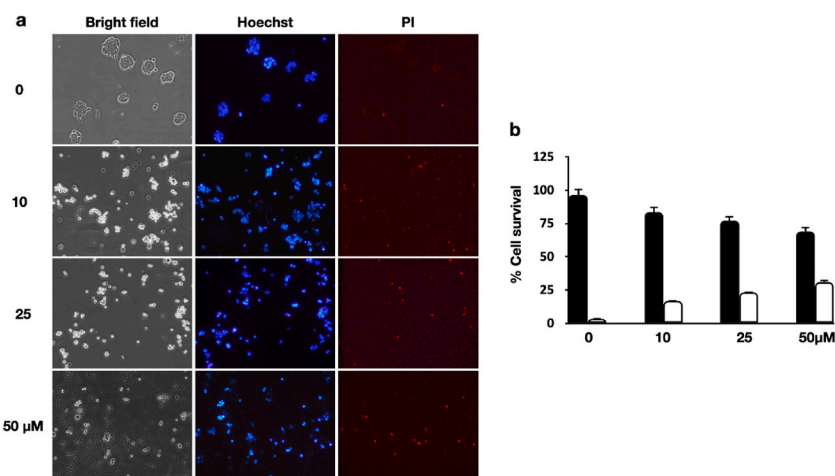

Fig. 14. Compound 7a effect on nuclear membrane deformation: Cells treated with various concentration of compound subjected to Hoechst/PI dual staining, (a) Hoechst/PI staining images, (b) histogram analysis of live and dead cells. DMSO treated cells served as control. Each experiment was repeated thrice error bars were represent the SEM of control with treated groups.

Table 4
The physicochemical properties of compound **7a** and standard drug (Gefitinib).

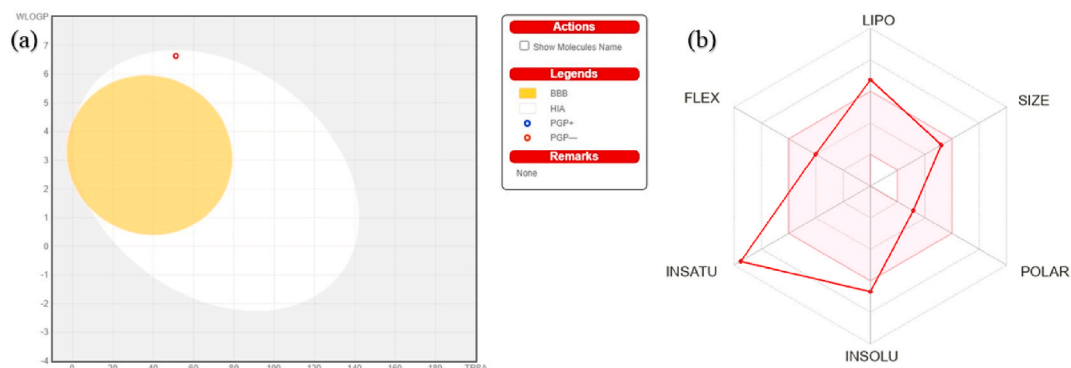| Compound name	MW	HBD	HBA	RB	lop p	Surface area $Å^2$
7a	430.507	1	3	5	6.8297	192.059
Gefitinib	446.91	1	7	8	4.2756	184.642

Fig. 15. (a) BOILED-EGG depicts gastrointestinal absorption and brain penetration of the compound **7a**. (b) The pharmacokinetic and Drug-Score of compound **7a** (The pink area represents the optimal range for each property). (For interpretation of the references to color in this figure legend, the reader is referred to the Web version of this article.)

chemistry are explored theoretically and experimentally, which enables us to create, investigate, and improve the biological activity of related compounds. By targeting PDK1, quinoline-4-carboxamide derivatives revealed strong antitumor effectiveness against colorectal cancer in an *in-vitro* assay, as evidenced by cell proliferation and viability assays. The substances successfully prevented the growth of colonies and caused apoptosis by activating caspase and deforming the nuclear membrane. Foci formation assay results demonstrated that the compounds effectively inhibited the colony formation capability of colon cancer cells. Hoechst/PI dual staining results unveiled the potent ability of compound to deform the nuclear membrane and induce apoptosis, as evidenced by increased caspases activation and changes in cell morphology. Molecular docking and molecular modeling studies indicated that the drug preferentially targeted the AKT pathway by inhibiting PDK1. The compound exhibited strong binding affinity with PDK1 active site amino acid residues by forming hydrogen bonds with TYR161 and THR222. Further, it was stabilized by π-π stacked interactions with LYS111, ALA109, VAL96, LEU88, VAL96 amino acids, with the binding energy of −10.2 kcal/mol, which was comparable to that of the standard medication drug Gefitinib (−7.1 kcal/mol). The results were substantiated by molecular dynamics studies, which also revealed strong interactions between ligand and protein over the simulation period of 100 ns. These findings suggest that quinoline-4-carboxamide derivatives could serve as a novel and effective strategy for cancer treatment, warranting further investigations and optimizations to enhance their therapeutic efficacy.

Data availability statement

Data will be made available on request.

Funding

Ethics declaration

Review and/or approval by an ethics committee as well as informed consent was not required for this study because this article did not involve any direct experimentation/studies on living beings.

CRediT authorship contribution statement

Shalini V: Writing – original draft, Visualization, Resources, Methodology, Formal analysis, Data curation, Conceptualization. **Priyadarshini A N:** Writing – original draft, Visualization, Validation, Methodology, Investigation, Formal analysis, Data curation, Conceptualization. **Harsha Kachigere B:** Validation, Methodology, Formal analysis, Data curation, Conceptualization. **Vinay Kumar D C:** Writing – original draft, Visualization, Validation, Software, Methodology, Investigation, Funding acquisition, Formal analysis, Data curation, Conceptualization. **Darshini Gowda:** Visualization, Validation, Resources, Methodology, Investigation,

Conceptualization. **Chethan B S:** Writing – original draft, Software, Resources, Methodology, Data curation. **Sudhanva M Srinivasa:** Writing – original draft, Visualization, Validation, Methodology, Investigation, Formal analysis, Data curation, Conceptualization. **Shobith Rangappa:** Writing – review & editing, Visualization, Validation, Supervision, Resources, Project administration, Funding acquisition. **Kanchugarakoppal S Rangappa:** Writing – review & editing, Visualization, Validation, Supervision, Software, Resources, Project administration, Methodology, Investigation, Funding acquisition, Formal analysis, Conceptualization.

Declaration of competing interest

The authors declare that they have no known competing financial interests or personal relationships that could have appeared to influence the work reported in this paper.

Acknowledgements

Appendix A. Supplementary data

Supplementary data to this article can be found online at https://doi.org/10.1016/j.heliyon.2024.e38105.

References

[1] H. Sung, J. Ferlay, R.L. Siegel, M. Laversanne, I. Soerjomataram, A. Jemal, F. Bray, Global cancer statistics 2020: GLOBOCAN estimates of incidence and mortality worldwide for 36 cancers in 185 countries, CA A Cancer J Clinicians 71 (2021) 209–249, https://doi.org/10.3322/caac.21660.

[2] A. Chao, M.J. Thun, C.J. Connell, M.L. McCullough, E.J. Jacobs, W.D. Flanders, C. Rodriguez, R. Sinha, E.E. Calle, Meat consumption and risk of colorectal cancer, JAMA 293 (2005) 172–182.

[3] G.A. Colditz, C.C. Cannuscio, A.L. Frazier, Cancer Causes and Control 8 (1997) 649–667, https://doi.org/10.1023/A:1018458700185 [No title found].

[4] Y. Ridouane, G. Lopes, G. Ku, H. Masud, B. Haaland, Targeted first-line therapies for advanced colorectal cancer: a Bayesian meta-analysis, Oncotarget 8 (2017) 66458.

[5] J.D. Sara, J. Kaur, R. Khodadadi, M. Rehman, R. Lobo, S. Chakrabarti, J. Herrmann, A. Lerman, A. Grothey, 5-fluorouracil and cardiotoxicity: a review, Ther Adv Med Oncol 10 (2018) 175883591878014, https://doi.org/10.1177/1758835918780140.

[6] I. Vivanco, C.L. Sawyers, The phosphatidylinositol 3-kinase–AKT pathway in human cancer, Nat. Rev. Cancer 2 (2002) 489–501.

[7] J. Brugge, M.-C. Hung, G.B. Mills, A new mutational AKTivation in the PI3K pathway, Cancer Cell 12 (2007) 104–107.

[8] Y. Samuels, L.A. Diaz, O. Schmidt-Kittler, J.M. Cummins, L. DeLong, I. Cheong, C. Rago, D.L. Huso, C. Lengauer, K.W. Kinzler, Mutant PIK3CA promotes cell growth and invasion of human cancer cells, Cancer Cell 7 (2005) 561–573.

[9] J.R. Testa, A. Bellacosa, AKT plays a central role in tumorigenesis, Proc. Natl. Acad. Sci. U.S.A. 98 (2001) 10983–10985, https://doi.org/10.1073/pnas.211430998.

[10] A. Narayanankutty, PI3K/Akt/mTOR pathway as a therapeutic target for colorectal cancer: a review of preclinical and clinical evidence, Curr. Drug Targets 20 (2019) 1217–1226.

[11] H. Huang, S. Park, H. Zhang, S. Park, W. Kwon, E. Kim, X. Zhang, S. Jang, D. Yoon, S.-K. Choi, J. Yi, S. Kim, Z. Dong, M. Lee, Z. Ryoo, M.O. Kim, Targeting AKT with costunolide suppresses the growth of colorectal cancer cells and induces apoptosis in vitro and in vivo, J. Exp. Clin. Cancer Res. 40 (2021) 114, https://doi.org/10.1186/s13046-021-01895-w.

[12] H.K. Roy, B.F. Olusola, D.L. Clemens, W.J. Karolski, A. Ratashak, H.T. Lynch, T.C. Smyrk, AKT proto-oncogene overexpression is an early event during sporadic colon carcinogenesis, Carcinogenesis 23 (2002) 201–205.

[13] S.M. Johnson, P. Gulhati, B.A. Rampy, Y. Han, P.G. Rychahou, H.Q. Doan, H.L. Weiss, B.M. Evers, Novel expression patterns of PI3K/Akt/mTOR signaling pathway components in colorectal cancer, J. Am. Coll. Surg. 210 (2010) 767–776.

[14] N. Dege, H. Gökce, O.E. Doğan, G. Alpaslan, T. Ağar, S. Muthu, Y. Sert, Quantum computational, spectroscopic investigations on N-(2-((2-chloro-4, 5-dicyanophenyl) amino) ethyl)-4-methylbenzenesulfonamide by DFT/TD-DFT with different solvents, molecular docking and drug-likeness researches, Colloids Surf. A Physicochem. Eng. Asp. 638 (2022) 128311.

[15] M. Gümüş, Ş.N. Babacan, Y. Demir, Y. Sert, İ. Koca, İ. Gülçin, Discovery of sulfadrug–pyrrole conjugates as carbonic anhydrase and acetylcholinesterase inhibitors, Archiv Der Pharmazie 355 (2022) 2100242, https://doi.org/10.1002/ardp.202100242.

[16] I. Mahmudov, Y. Demir, Y. Sert, Y. Abdullayev, A. Sujayev, S.H. Alwasel, I. Gulcin, Synthesis and inhibition profiles of N-benzyl-and N-allyl aniline derivatives against carbonic anhydrase and acetylcholinesterase–A molecular docking study, Arab. J. Chem. 15 (2022) 103645.

[17] M. Ilakiyalakshmi, A.A. Napoleon, Review on recent development of quinoline for anticancer activities, Arab. J. Chem. 15 (2022) 104168.

[18] A. Al Sheikh Ali, D. Khan, A. Naqvi, F.F. Al-Blewi, N. Rezki, M.R. Aouad, M. Hagar, Design, synthesis, molecular modeling, anticancer studies, and density functional theory calculations of 4-(1, 2, 4-triazol-3-ylsulfanylmethyl)-1, 2, 3-triazole derivatives, ACS Omega 6 (2020) 301–316.

[19] S. Sharma, S. Singh, D. Yadav, Quinoline-based anti-oncogenic molecules: synthesis and biological evaluation, Med. Chem. 19 (2023) 848–858.

[20] M.F. Mohamed, G.E.-D.A. Abuo-Rahma, Molecular targets and anticancer activity of quinoline–chalcone hybrids: literature review, RSC Adv. 10 (2020) 31139–31155.

[21] S. Banu, R. Bollu, R. Bantu, L. Nagarapu, S. Polepalli, N. Jain, R. Vangala, V. Manga, Design, synthesis and docking studies of novel 1, 2-dihydro-4-hydroxy-2-oxoquinoline-3-carboxamide derivatives as a potential anti-proliferative agents, Eur. J. Med. Chem. 125 (2017) 400–410.

[22] H.A. Blair, Pyrotinib: first global approval, Drugs 78 (2018) 1751–1755, https://doi.org/10.1007/s40265-018-0997-0.

[23] M.M. Elbadawi, W.M. Eldehna, W. Wang, K.K. Agama, Y. Pommier, M. Abe, Discovery of 4-alkoxy-2-aryl-6, 7-dimethoxyquinolines as a new class of topoisomerase I inhibitors endowed with potent in vitro anticancer activity, Eur. J. Med. Chem. 215 (2021) 113261.

[24] Z.S. El-Fakharany, Y.M. Nissan, N.K. Sedky, R.K. Arafa, S.M. Abou-Seri, New proapoptotic chemotherapeutic agents based on the quinolone-3-carboxamide scaffold acting by VEGFR-2 inhibition, Sci. Rep. 13 (2023) 11346.

[25] K. Ravi Singh, T.N. Lohith, T. Ananth Nag, M.A. Sridhar, M.P. Sadashiva, Structure property relationship in two thiazole derivatives: insights of crystal structure, Hirshfeld surface, DFT, QTAIM, NBO and molecular docking studies, Mol. Cryst. Liq. Cryst. (2023) 1–19.

[26] D.E. Pires, T.L. Blundell, D.B. Ascher, pkCSM: predicting small-molecule pharmacokinetic and toxicity properties using graph-based signatures, J. Med. Chem. 58 (2015) 4066–4072.

[27] D.V. Kumar, B.S. Chethan, V. Shalini, K.S. Rangappa, N.K. Lokanath, Structural elucidation and in-silico evaluation of 1, 2, 4-triazole derivative as potent Omicron variant of SARS-CoV-2 spike protein inhibitor with pharmacokinetics ADMET and drug-likeness predictions, J. Mol. Struct. (2023) 136976.

[28] İ. Çapan, S. Servi, İ. Yıldırım, Y. Sert, Synthesis, DFT study, molecular docking and drug-likeness analysis of the new hydrazine-1-carbothioamide, triazole and thiadiazole derivatives: potential inhibitors of HSP90, ChemistrySelect 6 (2021) 5838–5846, https://doi.org/10.1002/slct.202101086.

[29] G.M. Morris, R. Huey, W. Lindstrom, M.F. Sanner, R.K. Belew, D.S. Goodsell, A.J. Olson, AutoDock4 and AutoDockTools4: automated docking with selective receptor flexibility, J. Comput. Chem. 30 (2009) 2785–2791.

[30] J. Eberhardt, D. Santos-Martins, A.F. Tillack, S. Forli, AutoDock vina 1.2.0: new docking methods, expanded force field, and Python bindings, J. Chem. Inf. Model. 61 (2021) 3891–3898, https://doi.org/10.1021/acs.jcim.1c00203.

[31] Y. Sert, M. Gümüş, H. Gökce, İ. Kani, İ. Koca, Molecular docking, Hirshfeld surface, structural, spectroscopic, electronic, NLO and thermodynamic analyses on novel hybrid compounds containing pyrazole and coumarin cores, J. Mol. Struct. 1171 (2018) 850–866.

[32] D.S. Biovia, Discovery Studio Modeling Environment, Release, 2017.

[33] W.L. DeLano, The PyMOL Molecular Graphics System, 2002. Pymol. Org.

[34] D. Vinay Kumar, B. Chethan, D. Gowda, K. Rangappa, N. Lokanath, Investigation of the crystal structure, supramolecular architecture and in-silico myelofibrosis inhibition of a triazole derivative: a structural and theoretical approach, J. Mol. Struct. 1288 (2023) 135770.

[35] V. Kumar, S. Kumar, Ordering self-assembly structures via NH··· S and Br··· S interactions in (E)-2-(4-bromobenzylidene) hydrazinecarbothioamide: insights from crystallographic and computational study, J. Mol. Struct. 1310 (2024) 138285.

[36] S. Release, 1: Desmond Molecular Dynamics System, DE Shaw Research, Maestro-Desmond Interoperability Tools, Schrödinger, New York, NY, 2021, 2023.

[37] M.S. Zubair, S. Maulana, A. Widodo, R. Pitopang, M. Arba, M. Hariono, GC-MS, LC-MS/MS, docking and molecular dynamics approaches to identify potential SARS-CoV-2 3-chymotrypsin-like protease inhibitors from Zingiber officinale Roscoe, Molecules 26 (2021) 5230.

[38] Y.R. Girish, B.A. Kumar, K.S.S. Kumar, V.K. Hamse, K. Prashantha, M.S. Sudhanva, R. Shobith, Identification of novel benzimidazole-based small molecule targeting dual targets Tankyrase and Bcl2 to induce apoptosis in Colon cancer, J. Mol. Struct. 1269 (2022) 133813.

[39] J.G. Swathantraiah, S.M. Srinivasa, A.K. Belagal Motatis, A. Uttarkar, S. Bettaswamygowda, S.B. Thimmaiah, V. Niranjan, S. Rangappa, R.K. Subbegowda, T. N. Ramegowda, Novel 1,2,5-trisubstituted benzimidazoles potentiate apoptosis by mitochondrial dysfunction in panel of cancer cells, ACS Omega 7 (2022) 46955–46971, https://doi.org/10.1021/acsomega.2c06057.

[40] T.N. Lohith, S. Shamanth, M.A. Sridhar, K. Mantelingu, N.K. Lokanath, Synthesis, molecular structure, Hirshfeld surface, energy framework and DFT studies of 1, 3, 4 oxadiazole derivative, J. Mol. Struct. 1252 (2022) 132203.

[41] T.N. Lohith, K.R. Singh, C. Santhosh, M.A. Sridhar, M.P. Sadashiva, Rationalizing the stability and noncovalent interactions of N-(benzo [d][1, 3] dioxol-5-ylmethyl)-2-(methylthio) thiazole-4-carboxamide: insights from X-ray Structure and QTAIM Analysis, J. Mol. Struct. (2024) 139407.

[42] B.S. Chethan, H.R. Rajegowda, N.K. Lokanath, Structural and theoretical insights towards the understanding of the effect on the conformation of ligand by complexation process, J. Mol. Struct. 1276 (2023) 134759.